Pergamon

Int. J. Heat Mass Transfer. Vol. 38, No. 16, pp. 3035–3051, 1995

0017-9310/95 $9.50+0.00

0017-9310(95)00023-2

Influence of the heating rate on supercritical Rayleigh–Bénard convection

R. HERNÁNDEZ†

Universidad de Chile, Departamento de Ingeniería Mecánica Casilla 2777, Santiago, Chile

(*Received* 23 *February* 1994 *and in final form* 20 *December* 1994)

Abstract—The time dynamics of Rayleigh–Bénard convection originating from different heating rates for a Boussinesq fluid of Prandtl number $Pr = 0.71$ (air) has been studied numerically inside a three-dimensional (3D) rectangular box of aspect ratios $\Gamma_z = 1.25$, $\Gamma_y = 2$. The heating rate, introduced through a time dependent Rayleigh number $R(t)$, drives a flow transition at least in the range of supercritical Rayleigh numbers (R_s) here considered to solve the governing equations; $R_s = 3.6 \times 10^3$, 5×10^3, 9×10^3, 1.3×10^4 and 1.6×10^4. The flow transition, identified by a change of the rotation sense of a two-roll fluid pattern, was found when perfectly conducting side walls were used. This kind of flow transition has been reported in recent experiments.

INTRODUCTION

Rayleigh–Bénard (RB) convection is one of the simplest nonlinear problems where the velocity and temperature are coupled. RB convection is an appropriate model to understand the role of flow instabilities and laminar flow transitions [1]. The onset of RB convection has been widely investigated. For a review of the linear stability analysis, see Chandrasekhar [2]. For infinite parallel plates, there is a transition from a pure conductive regime to convection at the critical Rayleigh number $R_c = 1708$. The flow pattern consists of a series of counter rotating infinite rolls with axes parallel to the thermal active walls.

The finite box problem has been studied both experimentally and theoretically. The rectangular parallelepiped of Stork and Müller [3] and the right circular cylinder of Koschmieder [4] give us considerable information on both the onset of convection and the flow pattern found in RB convection for a wide range of aspect ratios of the confining container. In theory the predictions of Davis [5] agree very well with the experimental work of Stork and Müller [3], and the works on right cylinders of Koschmieder [4] and Stork and Müller [6] are in close concordance with the calculations of Charlson and Sani [7]. The flow pattern slightly above the critical R_c at moderate aspect ratios is time independent. However the flow pattern can exhibit temporal dependence for large aspect ratios [8].

Another feature of RB convection in confined enclosures is the loss of rolls or the wavelength increase when the Rayleigh number exceeds the critical value. The number of rolls is one of the most characteristic properties of RB convection. The number of rolls and the dimensionless wavelength λ, which corresponds to the ratio of the width of one roll to the depth d of the fluid layer, are inversely related. The theoretical computations of Schlüter *et al* [9] predict a decrease of the wavelength (increase of the number of rolls) with increasing supercritical Rayleigh number. Experimentally, however, the opposite result was found by Koschmieder [4] and Krishnamurti [10]. Furthermore, Mukutmoni and Yang [11] have shown through numerical computations that an increase of R beyond the critical value R_c affects significantly the steady flow pattern through the mechanism of loss of rolls. When the heating process in RB convection is made through a steady and fast increase of the temperature difference between the upper and lower plates, the wavelength also decreases [4]. This fact shows that the heating rate could be responsible for the change of pattern at a given supercritical Rayleigh number. In addition, Krishnamurti, through a theoretical and experimental work [12, 13] has shown that the slope η of a linear variation of the mean temperature can induce a different flow pattern depending on the value of η. At very low values of η the flow pattern was identified as 2D rolls and at high values of η hexagonal cells were found. Moreover, the sign of η was the controlling parameter of the direction of the flow at the center of the hexagonal cells. Recently, the experiments of Arroyo and Savirón [14] have shown that the rate of temperature increase leads to two different steady flow patterns in RB convection, which may be interpreted as two branches of a bifurcation.

In summary, the sensitivity of the convective pattern to the rate at which the heating is performed must be explored accurately in order to explain the physical mechanism responsible for that transition. In that

†Present address: Ecole Normale Supérieure de Lyon, Laboratoire de Physique. 46, Allée d'Italie, 69364 Lyon, France.

NOMENCLATURE

d depth of the fluid layer
g gravitational acceleration
l_x, l_y, l_z box dimensions in x, y, z coordinates, respectively
Nu local Nusselt number
$\langle Nu \rangle$ overall Nusselt number
Nu_m maximum local Nusselt number
p dimensionless pressure
Pr Prandtl number ν/α
q_x, q_y, q_z dimensionless heat fluxes at x, y, z directions, respectively
R Rayleigh number $g\beta\Delta T L_x^3/\nu\alpha$
R_c critical Rayleigh number at which convection starts
R_s supercritical Rayleigh number
$R(t)$ time dependent Rayleigh number $(R_s/\tau)\cdot t$
s_u, s_d flow states of the system
t dimensionless time
T_h, T_c hot and cold temperatures, respectively
u, v, w dimensionless velocity components at x, y, z coordinates, respectively
u_m, v_m, w_m maximum velocity componentes at x, y, z coordinates, respectively
$|\vec{v}|_m$ maximum velocity projection on a given plane of the velocity field
x, y, z dimensionless coordinates
u_i, x_i tensorial notation for velocity and coordinates, respectively.

Greek symbols
α thermal diffusivity
β coefficient of thermal expansion
Δt discrete time step
ΔT $(T_h - T_c)$ temperature difference
$\Delta T(t)$ time dependence of the temperature difference
$\Delta x, \Delta y, \Delta z$ discrete steps in x, y, z coordinates, respectively
$\Delta\Theta$ contour interval for isotherms
η slope of a linear variation of the mean temperature
Γ_y, Γ_z aspect ratios l_y/d and l_z/d, respectively
λ dimensionless wavelength
ν kinematic viscosity
Θ dimensionless temperature $(T-T_c)/(T_h-T_c)$
ρ fluid density
τ dimensionless duration of the unsteady heating
τ_r vertical relaxation time of the system d^2/α
τ_c critical value for τ
τ^-, τ^+ closest values of τ_c.

way, the full 3D nonlinear equations must be solved retaining time derivatives which suggests, due to their complexity, that a detailed numerical study could shed light on this phenomenon.

The goal of this work is to perform an accurate calculation of this kind of transition through a programmed temporal evolution of the governing equations. This can be done if one includes explicitly a time dependent Rayleigh number $R(t)$ in the governing equations. The $R(t)$ function will allow us to determine the influence of the heating rate (slope of the $R(t)$ function) on the flow pattern found for RB convection inside a small box.

In the present investigation, the governing equations for a Boussinesq fluid of Prandtl number $Pr = 0.71$ are integrated numerically in a 3D rectangular box of aspect ratios $\Gamma_z = 1.25$, $\Gamma_y = 2$ heated from below with perfect conductor side walls. A linear $R(t)$ function is considered, which has been already used [12, 15].

The fluid used in this analysis, characterized by its Prandtl number $Pr = 0.71$ (air), has been selected for its fast response to thermal changes (low thermal inertia).

The time dynamics of the convective regime originating from different heating rates shall be described at increasingly supercritical values of the Rayleigh number. In order to inspect the influence of the boundary conditions imposed at the side walls on the system behavior, an analysis shall be done for a similar physical configuration with adiabatic instead of perfect conductor side walls.

FORMULATION

Problem description

Consider a rectangular box of height $l_x = d$, horizontal dimensions l_y, l_z, of aspect ratios $\Gamma_y = l_y/d = 2$, $\Gamma_z = l_z/d = 1.25$ filled with a Boussinesq fluid of Prandtl number $Pr = 0.71$ (Fig. 1). The top and bottom boundaries are kept at temperatures T_c and T_h $(T_h > T_c)$, respectively and the side walls are perfect conductors.

The dimensionless governing equations in Cartesian coordinates for a Boussinesq fluid in three dimensions, neglecting radiation, are:

$$\frac{\partial u_i}{\partial x_i} = 0 \tag{1}$$

$$\frac{\partial u_i}{\partial t} + u_j \frac{\partial u_i}{\partial x_j} = -\frac{\partial p}{\partial x_i} + R_i Pr\theta + Pr[\nabla^2 u_i] \tag{2}$$

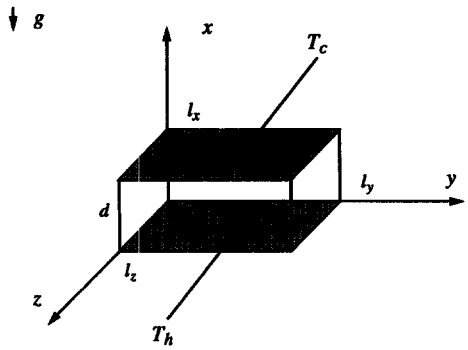

Fig. 1. Physical configuration.

$$\frac{\partial\theta}{\partial t}+u_i\frac{\partial\theta}{\partial x_i}=\nabla^2\theta. \tag{3}$$

The governing parameter is the time dependent Rayleigh number $R(t)=g\beta\Delta T(t)d^3/\nu\alpha$. The Prandtl number is $Pr=\nu/\alpha$, where α is the thermal diffusivity, ν the kinematic viscosity. $\Delta T(t)=T_h-T_c$ is the temperature difference between the top and bottom boundaries (which is a function of time), g the gravitational acceleration and β the thermal expansion coefficient.

Time, velocity, pressure and temperature are scaled using d^2/α, α/d, $\rho(\alpha/d)^2$ and (T_h-T_c), respectively, as reference quantities where ρ is the fluid density. The Cartesian coordinates are scaled with the height d of the cavity. The boundary conditions for the velocity and temperature in non dimensional form (u,v,w,θ) are the following:

$$\begin{aligned} y=0,\Gamma_y \quad & 0\leqslant x\leqslant\Gamma_x \quad 0\leqslant z\leqslant\Gamma_z \\ & u=v=w=0 \quad \theta=ltp \\ z=0,\Gamma_z \quad & 0\leqslant x\leqslant\Gamma_x \quad 0\leqslant z\leqslant\Gamma_y \\ & u=v=w=0 \quad \theta=ltp \\ x=0,1 \quad & 0\leqslant y\leqslant\Gamma_y \quad 0\leqslant z\leqslant\Gamma_z \\ & u=v=w=0 \quad \theta=1,0. \end{aligned}$$

At the vertical walls a linear temperature profile *ltp* between the temperature values of the hot and cold walls is imposed to emulate conduction [16].

The non dimensional heat transfer across the fluid is represented by the overall Nusselt number $\langle Nu\rangle$ which is computed, at each horizontal boundary, averaging the corresponding local Nusselt number Nu. The local Nusselt number is defined at any point of the physical domain by

$$Nu=\begin{cases} u\theta-\dfrac{\partial\theta}{\partial x} & x\text{ direction} \\ v\theta-\dfrac{\partial\theta}{\partial y} & y\text{ direction} \\ w\theta-\dfrac{\partial\theta}{\partial z} & z\text{ direction} \end{cases} \tag{4}$$

The numerical computation of the non-dimensional heat flux has been performed integrating the local Nusselt number, at each horizontal boundary of area Σ, using the following definition,

$$q=\int_\Sigma Nu\,d\sigma.$$

Note that at a given boundary the local Nusselt number definition in the normal direction must be used. The spatial derivatives involved in the Nusselt definitions have been computed with backward and forward two and three-point formulae and the Nusselt numbers were averaged using Simpson's rule.

Heating process and initial conditions

In RB convection experiments the heating process is normally a quasi-steady operation where the time involved to reach a determined supercritical Rayleigh number is many times greater than the thermal diffusion time scale or vertical relaxation time $\tau_r\equiv d^2/\alpha$ of the system.

Usually in the experiments, the fluid is first thermostated at a given temperature say T_0, next the upper plate is stabilized at T_0 to proceed to raise the lower plate temperature slowly, until a predetermined R_s is reached. In this way the final flow pattern is reached through a successive number of intermediate steady flow configurations where the system is in thermal and mechanical equilibrium. Therefore, the temporal dependence of $R(t)$ is attributed to the temporal variation of the temperature difference $\Delta T(t)$.

In this paper, the heating is a monotonic function of time which is introduced into the governing equations by means of a time dependent Rayleigh number $R(t)$ as follows:

$$R(t)=(R_s/\tau)\cdot t$$

where R_s is the prefixed supercritical value of R, t the dimensionless time and τ is a temporal dimensionless parameter which determines the slope and therefore the duration of the unsteady part of the heating process.

The choice of a linear time function for the heating process was made for convenience, however, it was already used in the theoretical works of Krishnamurti [12] and Swift and Hohenberg [15] and in the experimental work of Krishnamurti [13].

In order to simulate as closely as possible a real experiment, the calculation starts with a linear temperature profile between hot and cold wall (*ltp*) and the fluid at rest.

$$u(x,y,z,0)=v(x,y,z,0)=w(x,y,z,0)=0$$
$$\theta(x,y,z,0)=ltp \quad R(0)=0.$$

As the time progresses, the Rayleigh number is increased following the $R(t)$ function until the prefixed maximum value R_s is reached when $t=\tau$, then the programmed variation of $R(t)$ ends (unsteady part of the heating) and the time evolution of the system continues with $R(t)=R_s$. Note that the heating pro-

cess never ends because the forcing parameter $R(t)$ is always greater than zero.

NUMERICAL CONSIDERATIONS

Numerical method

The governing equations were solved in primitive variables. In the discretization of the physical domain a 3D, uniform and staggered grid was used with a control volume formulation and incorporating the SIMPLER algorithm of Patankar [17], with a power law scheme which has been previously used [18] to treat the convective–diffusive terms in the discrete formulation. The discrete equations were solved by an iterative tri-diagonal solver (TDMA) with additional criteria for fast convergence [19].

The time step Δt used in all calculations was 0.01, which represents 1% of the vertical relaxation time τ_r. A steady state solution, after the heating ends, required around 100 time steps which represent approximately 15 h of CPU on a SUN Sparc 690 server.

To ensure convergence of the numerical algorithm at each time step the following criteria were applied to all dependent variables at any grid location:

$$|\Phi_{ijk}^{m} - \Phi_{ijk}^{m+20}| \leqslant 10^{-3}$$

where Φ represents a dependent variable, the indexes i, j, k indicate a grid point and the index m a given iteration of the computer code. Also, the maximum residue of the discrete energy and momentum equations satisfied this convergence criteria.

In addition, an internal global check of accuracy and consistency is the energy balance. The heat fluxes over the box, which are computed using the heat flux definition of the preceding section, exhibit an overall residue which was always below 1.9% of the incoming heat flux at the bottom wall when steady state solutions arise. However, in some cases this residue was found to be less than 1%. If the convergence criteria is stretched, this residue can be minimized (up to machine precision), but the number of iterations required to solve the equations at a given time step increases surprisingly.

In this work a grid of $17 \times 21 \times 21$ points was used with $\Delta x = \Delta z = 0.0625$ and $\Delta y = 0.1$. A finer grid of $21 \times 41 \times 26$ points was also tested with a uniform step $\Delta x = \Delta y = \Delta z = 0.05$ to check if varying the grid spacing could increase the accuracy of the calculations. The results, which were obtained for $R_s = 5 \times 10^3$ and $\tau = 0.5$, indicate a relative difference from the first grid of 0.1% and 0.2% for the $\langle Nu \rangle$ averaged at the cold and the hot boundary, respectively. Additionally, the relative difference between both grids for the maximum vertical velocity is 1.8% and the overall heat flux residue falls below 1.3% of the incoming heat flux at the bottom boundary, which demonstrates an increased accuracy with finer grids. However, the required computational time to reach the steady state solution for the finest grid triples the corresponding time for the first grid. This suggests that the choice of the first grid to perform the calculations represents a good compromise between accuracy and computational effort.

Analytical solutions for 3D RB convection are not yet envisaged even for limiting cases. It therefore becomes necessary, in order to confirm the consistency and accuracy of the computer code, to reproduce previous experimental and numerical results if possible. The interferometric results of Farhadieh and Tankin [20] and the the numerical results of Fusegi *et al.* [21] were used for this purpose. Close agreement was found, indicating high accuracy of the code. The details of the validation are given elsewhere [18]. In addition, close agreement was found with the experimental results of Arroyo and Savirón [14], not only in the convective structure found but also in the critical behavior of the system, as will be seen in the next sections, although in [14] a fluid of high Prandtl number was used (silicon oil, $Pr = 130$).

NUMERICAL RESULTS

The heating rate which is controlled, at a fixed supercritical R_s, by the unsteady heating time τ produces an abrupt change in the steady flow pattern found in the box when different values of τ are considered. At a given supercritical Rayleigh number, the steady state flow pattern is characterized by two counter rotating rolls cells, with axes parallel to the shorter side of the box (l_z). This solution has already been found [3, 5, 11, 14].

At a fixed R_s, different slopes or heating rates will determine a very different flow structure. For example, when the steady state solution is reached at $R_s = 5 \times 10^3$ with $\tau = 1.4$ (Fig. 2 (a)), the convective motion between the two counter rotating rolls (central region) is oriented downward and upward near the side walls (system state s_d). On the other hand, when $\tau = 1.5$ (Fig. 2(b)), the fluid rises in the central region and falls near the side walls (system state s_u). This behavior agrees at least qualitatively well with the experimental results of Arroyo and Savirón [14]. Figure 2 presents the time evolution of the flow pattern and temperature field at $z = 0.5 l_z$ for s_d and s_u states of the system for $\tau = 1.4$, 1.5 and $R_s = 5 \times 10^3$. It is shown on x–y planes at $z = 0.5 l_z$. The time sequence ranges from pure conduction to the steady convection regime.

The convective motion has opposite direction depending on the value of the τ parameter. When the heating routine is made with $\tau = 1.4$, a descending flow appears at the central zone of the box, i.e. cold fluid falls. This cold flow increases with time due to the forcing parameter $R(t)$. At the same time, an ascending flow of hot fluid starts near the vertical walls by virtue of mass conservation and buoyancy forces, distorting the isotherms field at those regions. The same happens when $\tau = 1.5$ but in the opposite

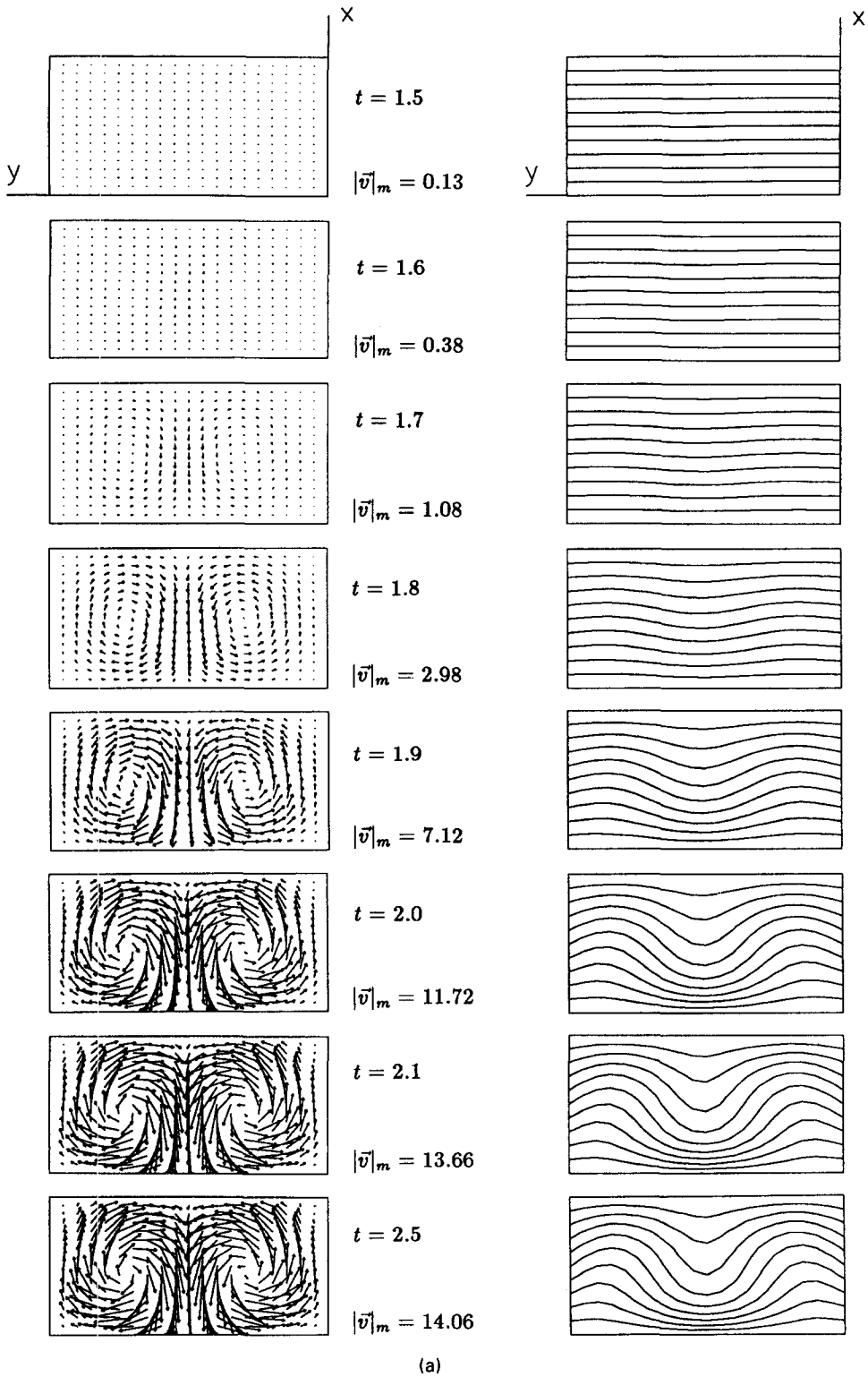

Fig. 2. Temporal evolution of the velocity field (left) and isotherms (right) at the middle plane of the box (plane x–y at $z = 0.5l_z$) at $R_s = 5 \times 10^3$. (a) $\tau = 1.4$, (b) $\tau = 1.5$. Contour interval for isotherms is $\Delta\theta = 0.1$. Time and maximum velocity projection $|\vec{v}|_m$ are shown. (*Continued overleaf.*)

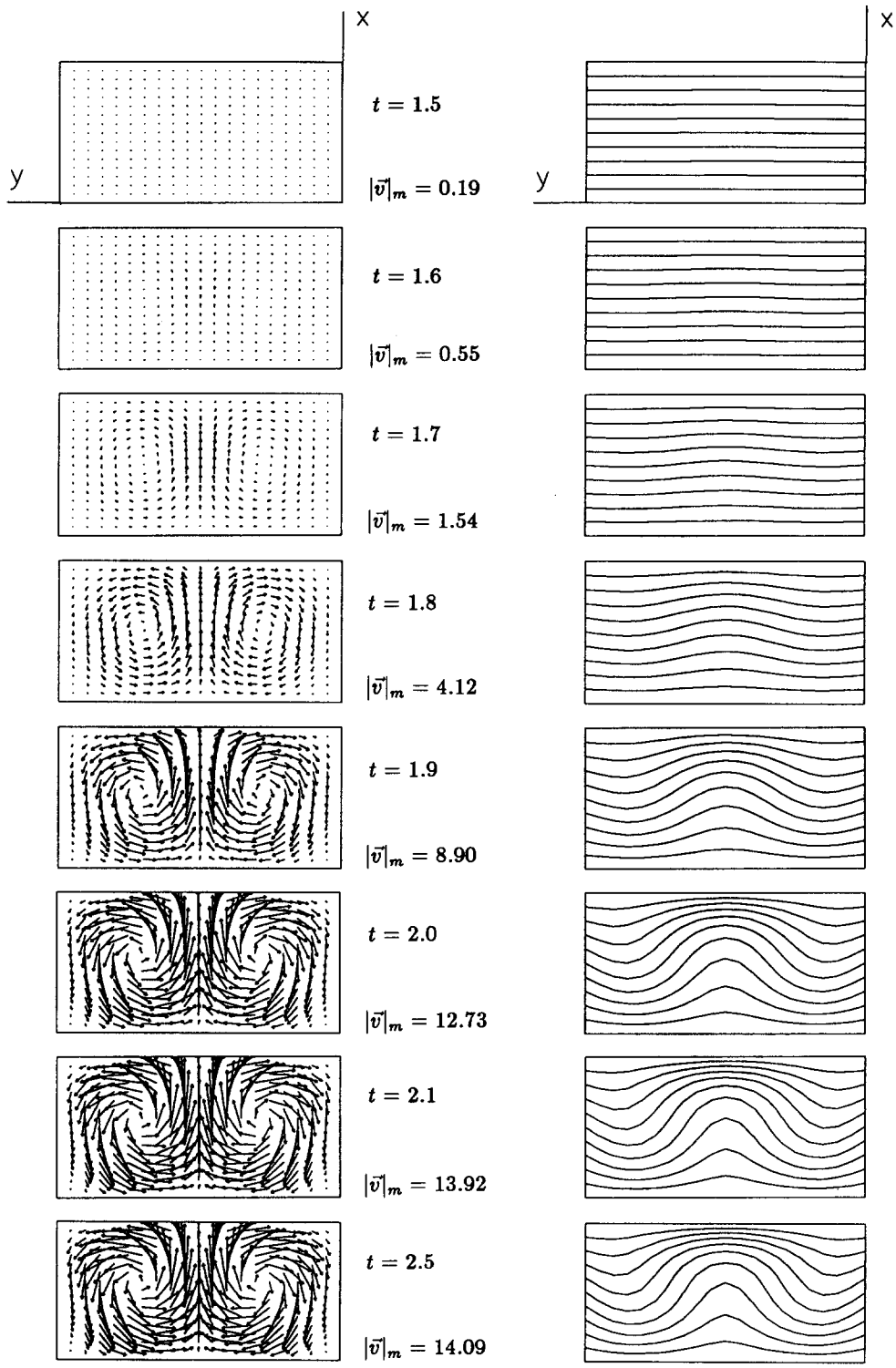

(b)

Fig. 2—*continued.*

direction. Hot fluid begins to ascend at the central region of the box causing a descending flow of cold fluid near the vertical walls which distorts the isotherms field in the opposite sense.

This system behavior is a flow transition clearly controlled by the parameter τ and it is possible, at least within the accuracy of the time step, to find the closest bounding values, here called τ^+ and τ^-, of the critical parameter τ_c at any given supercritical Rayleigh number R_s.

Flow pattern; dependence on R_s

At $R_s = 3.6 \times 10^3$ the fluid system is placed only slightly above the critical state characterized by R_c. The critical Rayleigh number for a box with similar dimensions is approximately $R_c \sim 3500$, as has been found experimentally by Stork and Müller [3].

The change of flow pattern found at this weak supercritical region is governed by the parameter τ. When $\tau \leqslant 1.05$, the u velocity becomes negative and two counter rotating rolls with a descending flow between them are observed (s_d system state). On the other hand, when $\tau \geqslant 1.06$, u becomes positive and two counter rotating rolls with an ascending flow between them are found (s_u system state). The system states, characterized by the flow pattern and the temperature field, obtained when $\tau \leqslant 1.05$, are identical. The same holds when $\tau \geqslant 1.06$.

This critical behavior can be seen in the sensitivity analysis of Fig. 3, which indicates the influence of τ in the case $R_s = 5 \times 10^3$. The vertical velocity u (Fig. 3(a)) and temperature θ (Fig. 3(b)) at the center of the box are plotted against time t for six values of τ. A family of identical s_d and s_u states is found when $\tau \leqslant 1.40$ and $\tau \geqslant 1.41$, respectively.

Although the overall convective behavior exhibited by the system is selected by the heating rate, after the unsteady heating process ends ($t = \tau$) the system begins to evolve towards an equilibrium state where the flow pattern and heat transfer does not present any variation with time t, indicating that the steady state has been reached (see for instance Fig. 3).

At higher supercritical Rayleigh numbers R_s the flow transition also occurs, which indicates that it is a robust change in the sense that it does not go away if the R_s is changed, at least in the R_s range here studied. Table 1 shows that the nearest bounding values τ^- and τ^+ of the critical parameter τ_c at which the system exhibits the flow transition are found to increase with higher values of R_s.

The overall flow pattern for all values of R_s is similar. However, the convective motion attributed to the velocities and heat transfer imposed by higher R_s is clearly stronger than at low R_s.

The increase of the convective motion of the system due to an increase of the Rayleigh number can be appreciated in Table 1, which shows the maximum velocities and local Nusselt numbers at each R_s when the s_d and s_u states arise for the five cases here studied. Owing to the strong increase of the vertical velocity, the horizontal velocities (v, w) begin to increase in order to preserve mass conservation in the whole physical domain. For instance, the maximum horizontal velocity w_m of the case $R_s = 3.6 \times 10^3$ is approximately 16% of the corresponding w_m of the case $R_s = 1.6 \times 10^4$ (see Table 1). In fact, an increase of the w component could be interpreted as an increase of flow three-dimensionality, but here this is not the case. As R_s grows, an important increase of the horizontal velocity components is found, but an increased region of a nearly 2D flow at the center of the box is also found (top view Fig. 5(b)).

Figure 4 summarizes the abrupt change in the direction of rotation of the rolls at each R_s tested in this work as a function of the τ parameter. The vertical velocity (Fig. 4(a)) and temperature (Fig. 4(b)) are plotted at the center of the box. The values of the parameter τ required to obtain the two directions of rotation at a given R_s are different. For instance, in cases where $\tau \geqslant \tau^+$, the increase of vertical velocity with the Rayleigh number R_s is obvious (a response of inertial terms to a thermal source term in momentum equations). In fact, it is caused by the overall increase of buoyancy forces which are proportional to $R(t)$. But the temperature behavior at the center is not obvious, because there is not a net increase when the steady state is reached. Looking at the s_u states (Fig. 4(b)), the minimum temperature at the center is obtained for the cases $R_s = 3.6 \times 10^3$ and $R_s = 1.6 \times 10^4$ (almost the same value) and the maximum temperature corresponds to the case $R_s = 5 \times 10^3$. This fact is instructive because it suggests that, as the R_s grows, the heat diffusion in horizontal direction becomes important (right-hand side of energy equation). This is a consequence of the presence of conducting side walls. The same occurs when $\tau \leqslant \tau^-$ cases are inspected. There is a decrease of the vertical velocity at the center of the box with R_s but the center temperature does not decrease continuously.

Figure 5 summarizes the five cases studied in this work. It shows for each R_s the velocity field and isotherms for x–y planes at $z = 0.5l_z$ and z–y planes near the top boundary ($x = 0.875$). Three main features of the convective motion must be explained. First, as R_s grows there is an increasing distortion of the isotherms at the side wall region caused by an ascending or descending flow depending on the τ value. A symmetric two-roll pattern can be seen which begins to align diagonally in the box. Viewing the z–y planes, one can note an increasingly 2D region with R_s, although there is an important increase of horizontal w velocity.

The temperature behavior at the center of the box, which has been mentioned before, can be understood by comparing the set of x–y isotherms. When τ^+ cases are considered, as the supercritical Rayleigh number R_s is increased, a portion of cold fluid coming from the top boundary begins to be directed towards the center of the box adopting a diagonal path. This trajectory will cool the center of the box, therefore

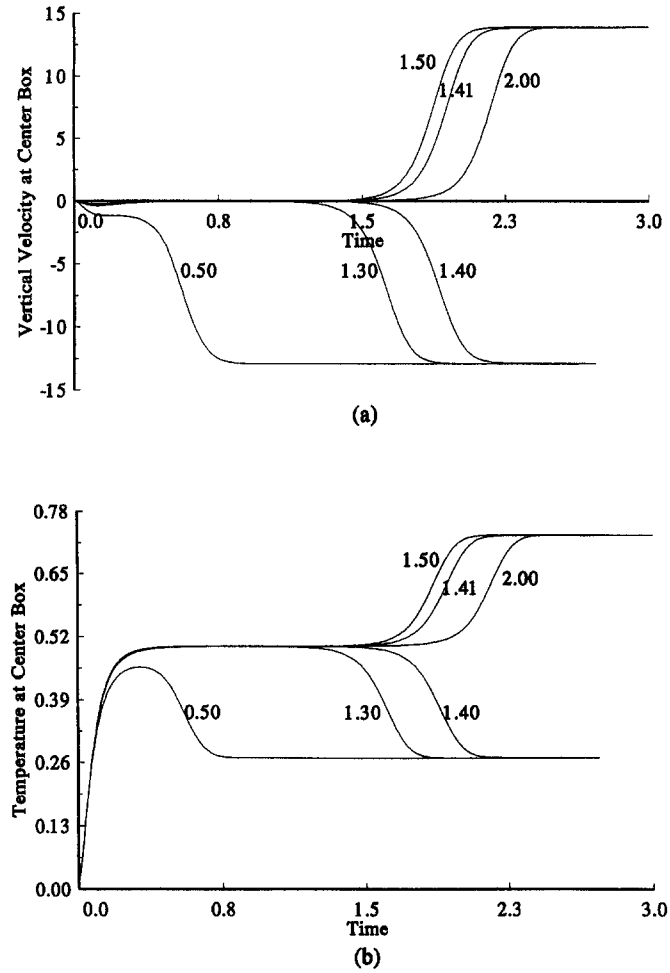

Fig. 3. Sensitivity analysis at $R_s = 5 \times 10^3$ as a function of the parameter τ at the center of the box for (a) vertical velocity u vs time t and (b) temperature θ vs time t. The different values of τ are printed over the curves.

Table 1. Absolute values for maximum velocities and local Nusselt numbers at both limits of τ_c

R_s	τ	u_m	v_m	w_m	Nu_m
3600	$\tau^- = 1.05$	7.60	4.07	2.07	2.88
	$\tau^+ = 1.06$	7.60	4.08	2.07	5.64
5000	$\tau^- = 1.40$	14.22	8.91	4.49	5.43
	$\tau^+ = 1.41$	14.25	8.83	4.51	10.37
9000	$\tau^- = 2.55$	22.42	17.33	7.41	9.47
	$\tau^+ = 2.56$	22.42	17.35	7.41	15.99
13000	$\tau^- = 3.68$	29.23	22.76	9.96	12.79
	$\tau^+ = 3.69$	29.26	22.72	10.11	20.77
16000	$\tau^- = 4.53$	33.77	25.94	12.06	14.90
	$\tau^+ = 4.54$	33.80	25.96	12.06	23.83

decreasing the local temperature. On the other hand, when τ^- cases are considered, a portion of hot fluid coming from the bottom boundary moves diagonally towards the center of the box and will increase the local temperature. In that way, the temperature behavior at the center of the box is a result of the diagonal fluid paths. The diagonal paths are caused by the thermal characteristics of the side walls (*ltp*

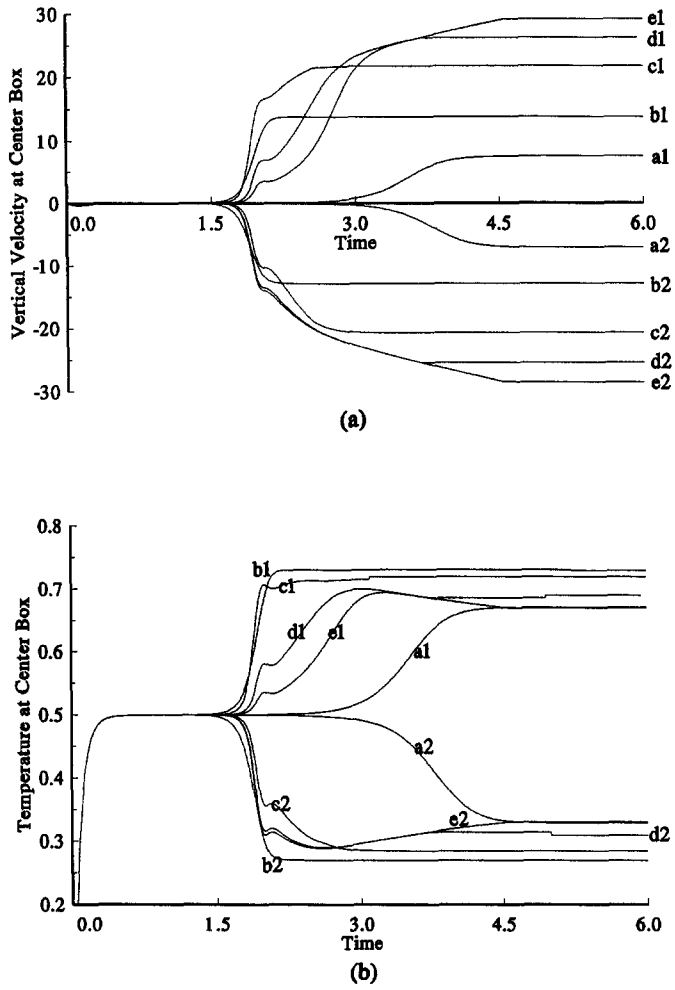

Fig. 4. Vertical velocity u (a) and temperature θ (b) at the center of the box as a function of time t when $\tau = \tau^-, \tau^+$ (subscripts 1, 2 respectively). $R_s = 3.6 \times 10^3$ (a1, a2), $R_s = 5 \times 10^3$ (b1, b2), $R_s = 9 \times 10^3$ (c1, c2), $R_s = 1.3 \times 10^4$ (d1, d2), $R_s = 1.6 \times 10^4$ (e1, e2).

profile). When a descending or ascending fluid flow starts near those walls, the distortion of the isotherms causes a horizontal heat flux which can be positive (incoming) or negative (outgoing). A positive heat flux will heat the descending cold fluid raising its local temperature and therefore its buoyancy forces. The increase of buoyancy and the proximity of the bottom boundary make the fluid turn horizontally, being incorporated to the ascending fluid path. On the other hand, when hot fluid ascends, a negative heat flux appears, decreasing its buoyancy forces gradually. This fact and the proximity of the upper boundary make the fluid turn horizontally to be incorporated this time to the descending fluid path. Physically, the increase or the decrease of buoyancy by way of the incoming and outgoing heat fluxes, respectively, has the effect of attenuating the fluid inertia, making the incorporation to the central fluid paths more easy.

Heat transfer

The most significant difference between the heat transfer map of the states s_d and s_u is the sense of the heat fluxes at each vertical wall of the box. When the heating routine provides a rising central flow (s_u), there exist three incoming heat fluxes into the box; at the bottom boundary and at the walls perpendicular to the roll axes or x–y walls. There are also three heat fluxes flowing out the box; at the top boundary and at the walls parallel to the roll axes or x–z walls. If the heating operation provides a system state s_d, the heat fluxes at the vertical walls have the opposite sense with respect to the s_u state. There exist incoming heat fluxes at the x–z walls and outgoing fluxes at the x–y walls (see Fig. 6).

This phenomenon, which was roughly explained in the preceding section, is attributed to the change of sign in the thermal gradient due to the convective

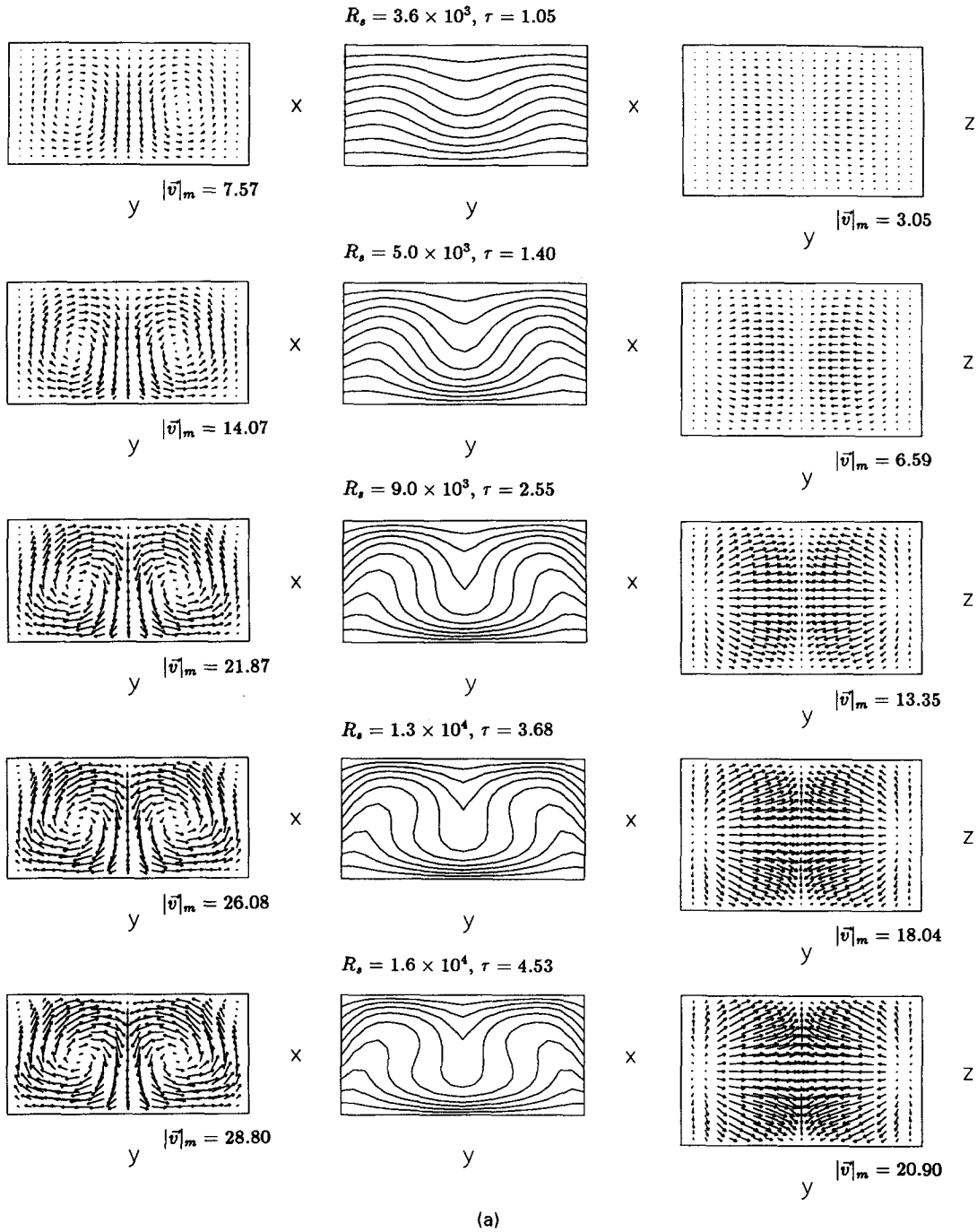

Fig. 5. Steady state velocity field (left) and isotherms (center) at the middle plane of the box (x–y at $z = 0.5l_z$) and velocity field (right) near top boundary (plane y–z at $x = 0.875$). (a) System state s_d with $\tau = \tau^-$. (b) System state s_u with $\tau = \tau^+$. Contour interval for isotherms is $\Delta\theta = 0.1$. Maximum velocity projection $|\vec{v}|_m$ is shown. (*Continued opposite.*)

distortion that the thermal field undergoes near the vertical walls. At the vicinity of x–z walls the slope of isotherms will be negative (inclined towards the hot boundary) when system state s_u is considered, because cold fluid descends near these zones. Therefore, the thermal gradient in the horizontal direction will generate an incoming heat flux. On the other hand, when the system reaches the state s_d, the rising flow near the x–y walls makes the slope of isotherms positive (inclined towards the cold boundary), then the thermal gradient points out from the walls, producing an outgoing heat flux.

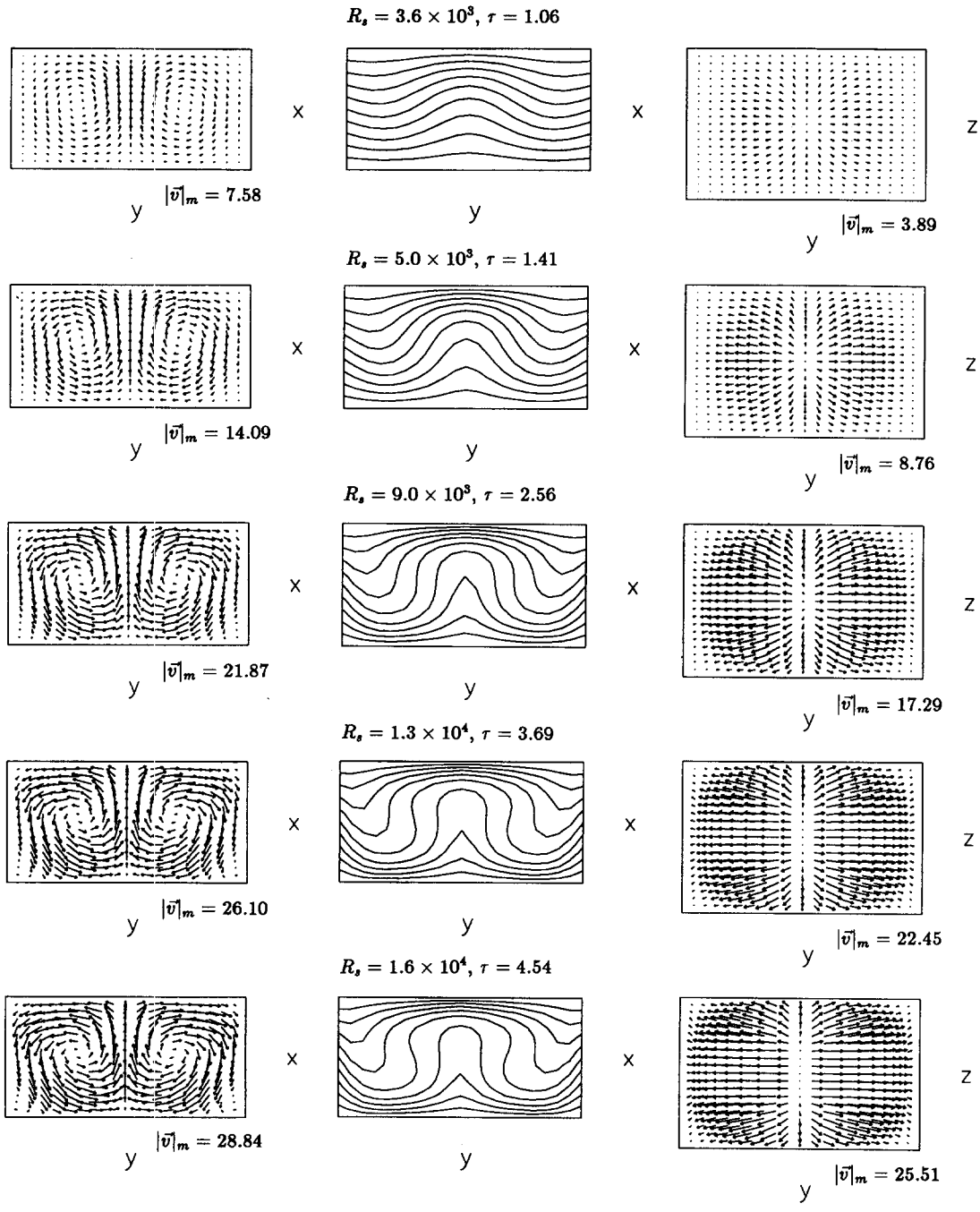

(b)

Fig. 5—*continued.*

When x–y walls are considered, the alternation of heat fluxes, between s_u and s_d states, obeys the same rule, but is slightly different. The change of slope of the isotherms is also caused by the moving fluid. But at a given heating rate, the x–y walls present both negative and positive signs of the thermal gradient, because they are exposed to an ascending and a descending flow at the same time, independently of the heating routine. This makes the average heat exchange between the fluid and those walls, if not zero, less important than at the other walls because cancellation of heat fluxes will occur in the average operation.

As R_s grows, an increase of all heat fluxes is found, but the vertical heat fluxes are always greater than the other ones. However, the ratio between lateral and vertical heat fluxes also increases and for instance, the

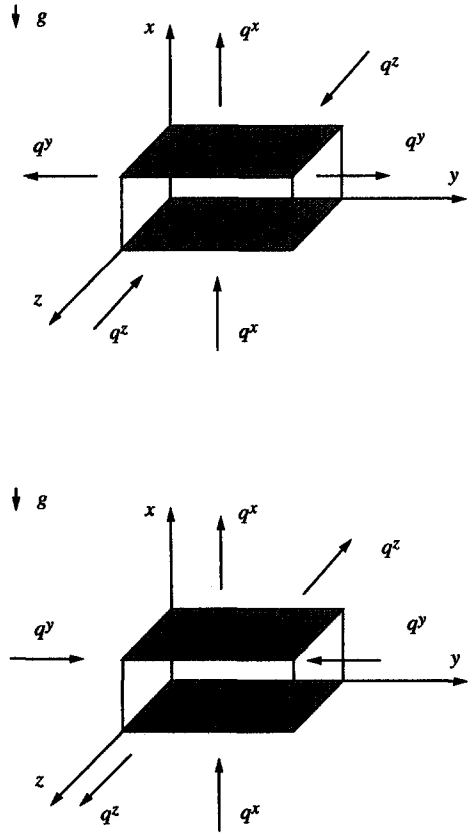

Fig. 6. Schematic heat fluxes. (a) System state s_d, $\tau = \tau^-$. (b) System state s_u, $\tau = \tau^+$.

percentage of the heat flux at x–y walls with respect to the incoming heat flux at bottom boundary was increased from $R_s = 3.6 \times 10^3$ to $R_s = 1.6 \times 10^4$ by approximately 5–14%, respectively. Physically, higher vertical velocities near lateral walls produce a higher distortion of the isotherms, which will increase the rate of heat exchange.

At a determined R_s value, the absolute values of the heat fluxes at the side walls are almost the same when s_u and s_d states are considered, and the heat fluxes at top and bottom walls are inverted, i.e. the top heat flux value when $\tau = \tau^-$ coincides approximately with the bottom heat flux when $\tau = \tau^+$ and vice versa. This fact with the help of the maximum velocity values sketched in Table 1 indicates that both s_u and s_d states are symmetrical under a transformation $x \to l_x - x$ and $u \to -u$.

The generalized increase of convective motion exhibited by the system with increasing values of R_s can also be seen in Fig. 7 where the overall Nusselt number $\langle Nu \rangle$ at the top and bottom boundary is plotted against time when the system adopts the s_d state (s_u state is not shown). In the transient part of these graphs there is an almost fixed region where $\langle Nu \rangle = 1$ indicating a pure conductive thermal regime followed by a convective regime which starts at approximately the same point for all R_s with the exception of case $R_s = 3.6 \times 10^3$ where the pure conductive regime has a large extent. This behavior can also be noted in Fig. 4, where the pure conductive regime is distinguished by the values adopted by the vertical velocity and temperature at the center of the box ($\theta = 0.5$ and $u = 0$) in all cases.

Adiabatic vs perfect conductor side walls; flow transition

This singular flow transition depends on the thermal boundary conditions imposed at vertical walls. When one considers adiabatic (A) instead of perfect conductor (C) side walls, and starts the calculation with the same initial conditions, the flow pattern found does not change when τ is varied, i.e. the flow transition disappears, at least in the R_s range here considered.

The flow pattern found always consist of two counter rotating rolls with axes parallel to the shorter side of the box. Hot fluid rises at the center of the box and cold fluid sinks near the side walls. Therefore the adiabatic roll pattern is closely similar to the perfect conductor case in the s_u state (in a dynamical sense).

Figure 8 shows the steady state velocity field and isotherms for an adiabatic and a perfect conductor case. It shows the x–y plane at $z = 0.5 l_z$ and the z–y plane near the top boundary ($x = 0.875$). The Rayleigh number is $R_s = 5 \times 10^3$ and the parameter τ is $\tau = 0.5$. Grace $\tau < \tau^-$ the system in the perfect conductor case exhibits a s_d state which is the opposite of the adiabatic case. But a major difference arises when the isotherms are compared. The boundary condition at side walls for the adiabatic case forbids heat transfer between the fluid and the environment, and the incoming heat flux at the bottom boundary is convected entirely towards the upper plate.

The effectiveness of the adiabatic case to carry heat from plate to plate is confirmed in Fig. 9, where for $R_s = 5 \times 10^3$, the adiabatic case ($\tau = 0.5$) and the perfect conductor case exhibiting s_u states ($\tau = 1.41$), are compared. The overall Nusselt number of the adiabatic case at the bottom or top boundaries is always greater than in the perfect conductor situation (Figs. 9(a) and (b)). In addition, Fig. 10(a) shows that the adiabatic case has a greater vertical velocity at the center of the box than in the perfect conductor case, although the local temperature at the same location does not differ (Fig. 10(b)). It is clear from the arguments given above, that the flow transition driven by the critical parameter, here referred to as τ_c, is dependent on the boundary conditions imposed at the side walls.

The comparison between both physical configurations suggests that the mechanism responsible for the flow transition at a given R_s is the competition between the side wall and horizontal boundary conditions. The buoyancy forces generated by the *ltp* con-

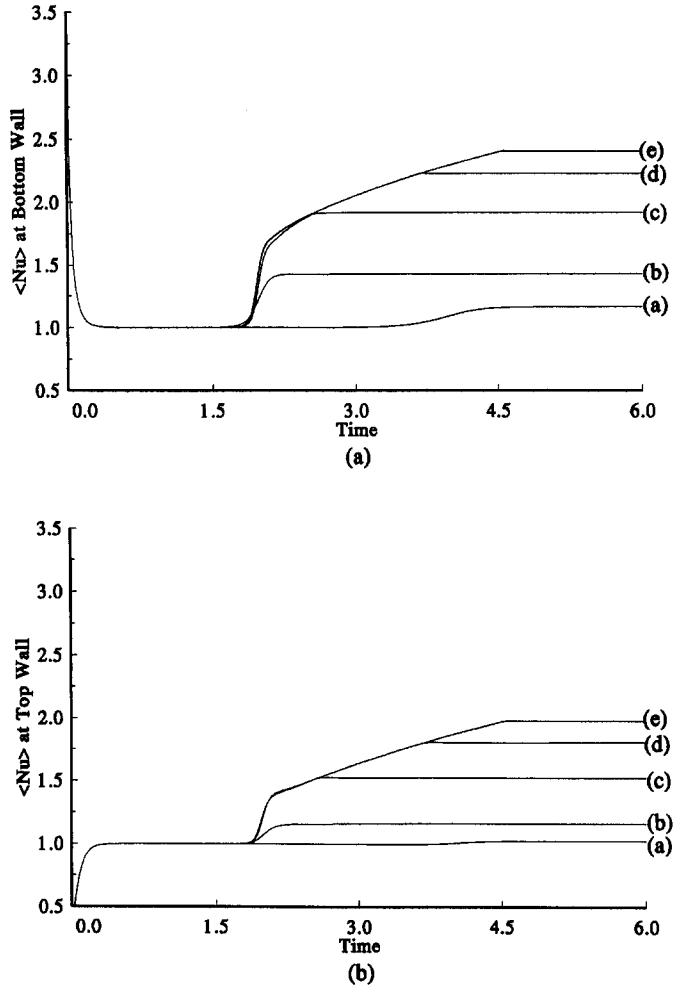

Fig. 7. Overall Nusselt number $\langle Nu \rangle$ as a function of time t when system state is s_d. (a) Top boundary. (b) Bottom boundary. $R_s = 3.6 \times 10^3$ (a), $R_s = 5 \times 10^3$ (b), $R_s = 9 \times 10^3$ (c), $R_s = 1.3 \times 10^4$ (d), $R_s = 1.6 \times 10^4$ (e).

dition imposed at the side walls will always drive a rising flow near these walls, independently of the Rayleigh number ($R_s > 0$), when combined with adiabatic horizontal walls [22].

However, when the box is heated from below and the side walls are considered adiabatic, the convective motion starts when the Rayleigh number reaches the critical value R_c. On the other hand, when a box heated from below has *ltp* side walls, a rising flow near vertical walls accompanied by a downward flow at the box center (s_d state) would be observed for $R(t) < R_c$. This argument can be confirmed in Fig. 10(a) where a weak negative vertical velocity, during a short time interval, is observed at the center of the box in the perfect conductor case, indicating a very weak primary s_d state. However this state is then neutralized by virtue of the increase of buoyancy of the central flow, and therefore vanishes, giving rise a pure conductive regime.

This regime will be dominant until the critical Rayleigh number is reached. Then the convective pattern starts either as an s_d or s_u state selected by τ^- or τ^+, respectively. Figures 3(a) and 4(a) also show the presence of the weak primary convection. This phenomenon is present in all cases independent of the final supercritical Rayleigh number (Fig. 4(a)). Thus the physical mechanism driving the flow transition can be regarded as the competition of buoyancy forces generated near side walls against those generated at the central region of the box when the critical state is reached. For $\tau < \tau_c$ convection starts near side walls and for $\tau > \tau_c$ the fluid motion will start at the central region giving rise to an s_d and an s_u state, respectively.

The computed values τ^- and τ^+ which determine s_d and s_u states at every R_s are, as was mentioned before, the nearest bounding values of the critical parameter τ_c allowed by the time step accuracy. In principle, a best approximation to τ_c could be possible with finer time steps, however, the restriction imposed by the

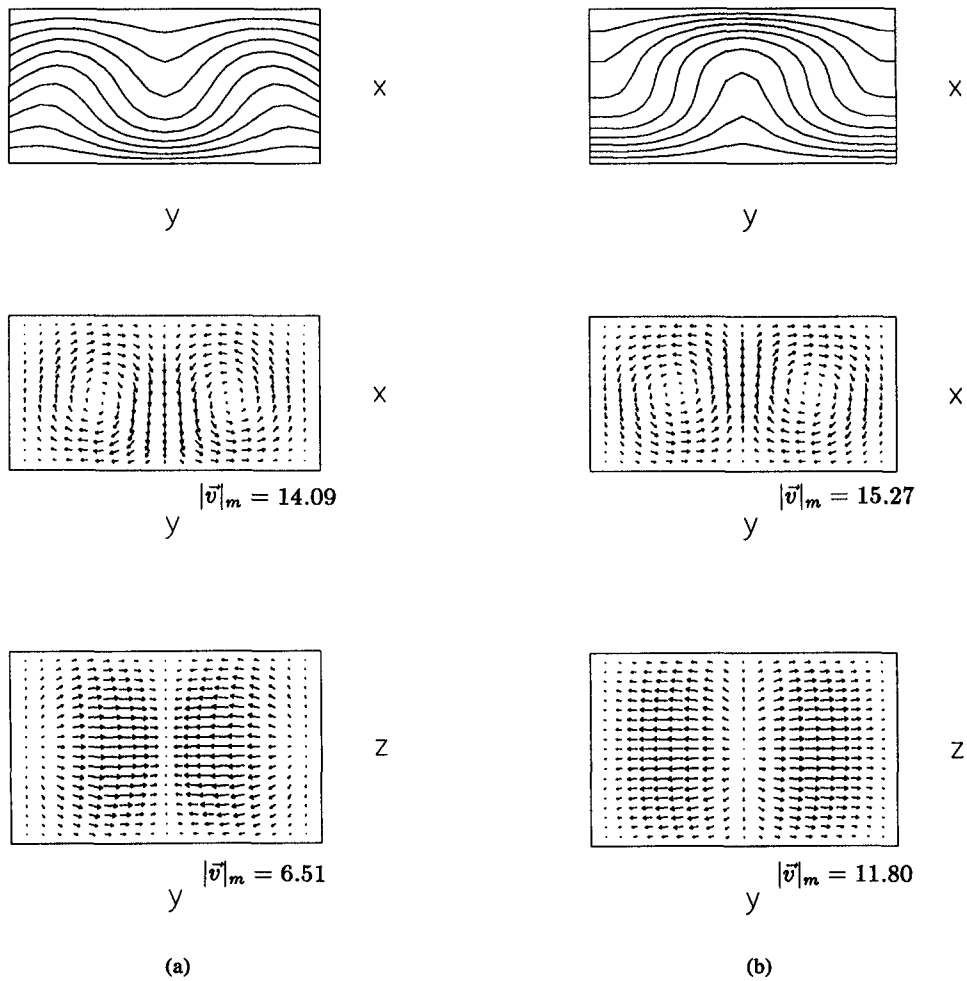

Fig. 8. Steady state velocity field (center) and isotherms (top) at the middle plane of the box (x–y at $z = 0.5l_z$) and velocity field (bottom) near the top boundary (plane y–z at $x = 0.875$). (a) Case of perfect conductor side walls, $R_s = 5 \times 10^3$ and $\tau = 0.5$. (b) Case of adiabatic side walls, $R_s = 5 \times 10^3$ and $\tau = 0.5$. Contour interval for isotherms is $\Delta\theta = 0.1$. Maximum velocity projection $|\vec{v}|_m$ is shown.

machine precision and especially the excessive computing time forbids the numerical search of τ_c.

Finally, one further remark. The overall behavior exhibited by τ^-, τ^+ and therefore by τ_c behind the values of R_s of Table 1, shows that as R_s approaches the critical Rayleigh number (Stork and Müller [18]), the bounding limits of τ_c decrease and for R_s close to R_c ($R_s = 3.6 \times 10^3$) τ^- and τ^+ are found close to unity. In other words, for the lowest R_s value here investigated, the critical parameter is close to the vertical relaxation time of the system $\tau_c \sim \tau_r$. This fact suggests a tendency of the critical parameter, $\tau_c \to \tau_r$ when $R_s \to R_c$, but it is not possible here to assume it because lower R_s values were not considered because they need an increased time step resolution in order to detect the flow transition.

CONCLUDING REMARKS

A detailed numerical study of the Rayleigh–Bénard problem in a 3D box of aspect ratios $\Gamma_y = 2$ and $\Gamma_z = 1.25$ has been made. The flow pattern found at different values of the supercritical Rayleigh number R_s consists of two counter rotating roll cells with axes parallel to the shorter dimension of the box (l_z).

It has been found that the heating rate, which is incorporated into the governing equations by way of a time dependent Rayleigh number $R(t)$, drives a robust flow transition (in the sense that it does not go away when R_s is increased), when the Rayleigh number is assumed a linear function of time. The flow transition, which could also be interpreted as the two branches of a flow bifurcation, consists of an abrupt change in

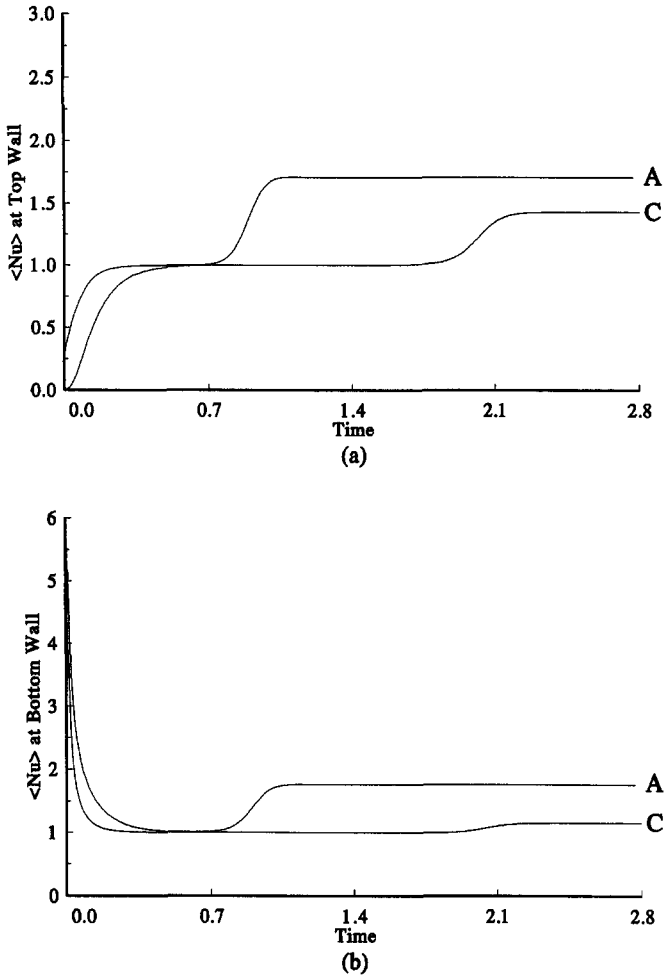

Fig. 9. Adiabatic side walls (A) vs perfect conductor side walls (C). (a) Overall Nusselt number $\langle Nu \rangle$ at the top boundary. (b) Overall Nusselt number $\langle Nu \rangle$ at the bottom boundary.

the sense of rotation of the two-roll pattern when the unsteady heating time or τ parameter is located below (system state s_d) and above (system state s_u) a critical value, here referred as τ_c, respectively. The exact values of τ_c were not found, however their bounding limits, referred as τ^-, τ^+, were obtained within time step accuracy at every R_s.

The flow transition is dependent on the boundary conditions imposed at the side walls. When adiabatic instead of perfect conductor side walls are considered, the flow transition does not appear. This fact suggest that the mechanism driving the flow transition takes form from the competition of lateral against central buoyancy forces when the system approaches the critical state. The value of τ (unsteady heating rate) determines the predominance of one local region over the other.

As R_s grows, an important increase of the horizontal velocity components is found, but an increased region of nearly 2D flow at the center of the box is also found.

The behavior of the heat transfer at the two sides of the flow transition is different. At a given R_s the direction of the heat flux at the vertical walls found at state s_u is the opposite of the direction in the state s_d. Additionally, the magnitude of the heat flux that leaves the box through the upper plate in the s_u state is very similar to the magnitude of the incoming heat flux at the bottom boundary when the system is in the s_d state, which suggests, in conjunction with the similarity of the maximum velocities found, that both states are approximately symmetrical with respect to a transformation $x \to l_x - x$ and $u \to -u$.

Finally, as R_s approaches the critical Rayleigh number, the bounding limits of τ_c are found close to the vertical relaxation time of the system τ_r.

Acknowledgements—The author wishes to thank Professors R. L. Frederick and F. Lund for constructive comments on the manuscript and to Mr. V. Borquez for many helpful discussions. Part of this work was supported by FONDECYT Grant 1265-91 and CEC contract CI1*CT910947.

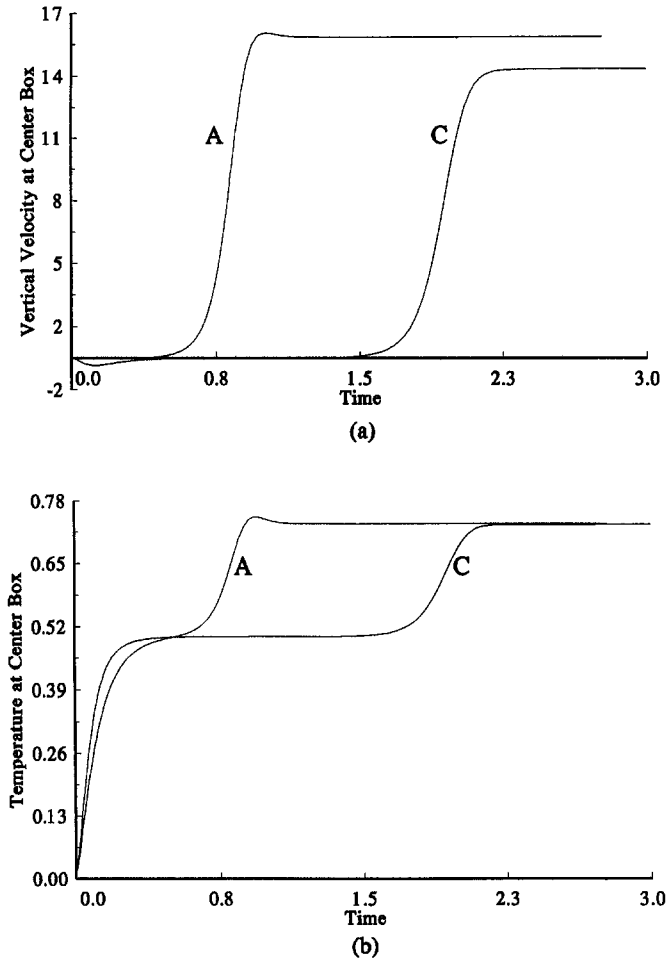

Fig. 10. Adiabatic side walls (A) vs perfect conductor side walls (C). (a) Vertical velocity u at the center of the box. (b) Temperature θ at the center of the box.

REFERENCES

1. C. Normand, Y. Pomeau and M. G. Velarde, Convective instability: a physicist's approach, *Rev. Modern Phys.* **49,** 581–624 (1977).
2. S. Chandrasekhar, *Hydrodynamic and Hydromagnetic Stability*, Chap. II. Dover Publications, New York (1981).
3. K. Stork and U. Müller, Convection in boxes: experiments, *J. Fluid Mech.* **54**(4), 599–611 (1972).
4. E. L. Koschmieder, On the wavelength of convective motions, *J. Fluid Mech.* **35**(3), 527–530 (1969).
5. S. H. Davis, Convection in a box: linear theory, *J. Fluid Mech.* **30**(3), 465–478 (1967).
6. K. Stork and U. Müller, Convection in boxes: an experimental investigation in vertical cylinders and annuli, *J. Fluid Mech.* **71**(2), 231–240 (1975).
7. G. S. Charlson and R. L. Sani, Thermoconvective instability in a bounded cylindrical fluid layer, *Int. J. Heat Mass Transfer* **13,** 1479–1496 (1970).
8. G. Alhers, D. S. Cannell and V. Steinberg, Time dependence of flow patterns near the convective threshold in a cylindrical container, *Phys. Rev. Lett* **54,** 1373–1376 (1985).
9. A. Schlüter, D. Lortz and F. Busse, On the stability of steady finite amplitude convection, *J. Fluid Mech.* **23,** 129–144 (1965).
10. R. Krishnamurti, On the transition to turbulent convection—1. The transition from two- to three-dimensional flow, *J. Fluid Mech.* **42**(2), 295–307 (1970).
11. D. Mukutmoni and K. T. Yang, Wave number selection for Rayleigh–Bénard convection in a small aspect ratio box, *Int. J. Heat Mass Transfer* **35**(9), 2145–2159 (1992).
12. R. Krishnamurti, Finite amplitude convection with changing mean temperature—1. Theory, *J. Fluid Mech.* **33**(3), 445–455 (1968).
13. R. Krishnamurti, Finite amplitude convection with changing mean temperature—2. An experimental test of the theory, *J. Fluid Mech.* **33**(3), 457–463 (1968).
14. M. P. Arroyo and J. M. Savirón, Rayleigh–Bénard convection in a small box: spatial features and thermal dependence of the velocity field, *J. Fluid Mech.* **235,** 325–348 (1991).
15. J. B. Swift and P. C. Hohenberg, Rayleigh–Bénard convection with time-dependent boundary conditions, *Phys. Rev. A* **39**(8), 4132–4136 (1989).
16. S. M. Elsherbiny, K. G. T. Hollands and G. D. Raithby, Effect of thermal boundary conditions on natural con-

vection in vertical and inclined air layers, *ASME J. Heat Transfer* **104,** 515–520 (1985).
17. S. V. Patankar, *Numerical Heat Transfer and Fluid Flow*. Hemisphere, Washington D.C. (1980).
18. R. Hernández and R. L. Frederick, Spatial and thermal features of Rayleigh–Bénard convection, *Int. J. Heat Mass Transfer* **37**(3), 411–424 (1994).
19. J. P. Van Doormaal and G. D. Raithby, Enhancements of the simple method for predicting incompressible fluid flows, *Numer. Heat Transfer* **7,** 147–163 (1984).
20. R. Farhadieh and R. S. Tankin, Interferometric study of two-dimensional Bénard convection cells, *J. Fluid Mech.* **66,** 739–752 (1974).
21. T. Fusegi, J. M. Hyun, K. Kuwahara and B. Farouk, A numerical study of three-dimensional natural convection in differentially heated cubical enclosure, *Int. J. Heat Mass Transfer* **34**(6), 1543–1557 (1991).
22. K. T. Yang, Transitions and bifurcations in laminar buoyant flows in confined enclosures, *ASME J. Heat Transfer* **110,** 1191–1204 (1988).